Supplementary Information

Additive Manufacturing of Patterned 2D Semiconductor through Recyclable Masked Growth

Yunfan Guo[1], Pin-Chun Shen[1], Cong Su[2], Ang-Yu Lu[1], Marek Hempel[1], Yimo Han[3], Qingqing Ji[1], Yuxuan Lin[1], Enzheng Shi[4], Elaine McVay[1], Letian Dou[4], David A. Muller[3], Tomás Palacios[1], Ju Li[2], Xi Ling[5*], Jing Kong[1*]

[1]Department of Electrical Engineering and Computer Science, Massachusetts Institute of Technology, Cambridge MA 02139, USA

[2]Department of Nuclear and Materials Science and Engineering, Massachusetts Institute of Technology, Cambridge MA 02139, USA

[3]School of Applied & Engineering Physics, Cornell University, Ithaca, New York 14850, USA

[4]Davidson School of Chemical Engineering, Purdue University, West Lafayette, IN 47907, USA

[5]Department of Chemistry, Division of Materials Science and Engineering, and The photonics Center, Boston University, Boston, MA 02215, USA

www.pnas.org/cgi/doi/10.1073/pnas.1816197116

Supplementary Text

Characterization: AFM characterization was conducted on a Dimension 3100 instrument, from VEECO Instruments Inc. Raman and PL spectra were carried out on a Horiba Jobin-Yvon HR800 system and a Witec Alpha300-confocal Raman Microscope. The laser excitation wavelength for Raman and PL measurements were 532.5 nm. Laser power was about 0.1 mW. A 50X objective was used to focus the laser beam. For PL and Raman mapping, the scanning step sizes are 0.8 μm on a Horiba HR800 system, and 0.3 μm on a Witec Alpha 300-confocal Raman Microscope. The atomic structure of the sample was acquired by imaging using an aberration corrected Nion UltraSTEM100. The sample was baked in vacuum under 160°C for 8 hours before insertion into the microscope chamber. The electron acceleration voltage was kept at 60 kV during the operation to avoid the knock-on damage during imaging. The vacuum level during the experiments was kept under 3×10^{-9} mbar. The convergence angle of electron probe is 60 mrad and the collection angle of the high angle annular dark field (HAADF) is 70-200 mrad.

Device Fabrication and Measurement: Patterned monolayer MoS_2 nanostructures were first transferred onto 300 nm SiO_2/p+-Si substrates by the PMMA transfer method. E-beam lithography (EBL), e-beam evaporation followed by a lift-off process were used to deposit Ni/Au (30/20 nm) as electrodes. Since all devices are based on patterned monolayer MoS_2 nanostructures, there is no need to use oxygen plasma to isolate the channel area. The transport measurements were carried out under ambient environment at room temperature using a semiconductor parameter analyzer (Agilent 4155C) and a cryogenic probe station (Lakeshore).

FET Device based on patterned monolayer MoS_2. The linear output characteristics demonstrate that Ohmic-like contact is achieved at the interface. We extract the mobility of the MoS_2 FET using Equation (1).

$$\mu_{FE} = \frac{L_{ch}}{W_{ch}\, C_{ox}\, V_{ds}} \frac{dI_{ds}}{dV_{bg}} \quad (1)$$

where C_{ox} is the gate capacitance, L_{ch} (= 2 μm) and W_{ch} (= 10 μm) are channel length and width, respectively. The contact resistance (R_c) of our MoS_2 FETs was further extracted based on the transfer length method. Fig. 1*J* shows a linear fit to the total resistance normalized by channel width (R_{TOT}) versus L_{ch}, of which the vertical intercept yields the total contact resistance ($2R_c$). The carrier density *n* is estimated by a linear charge dependence on the gate voltage overdrive

$$n = \frac{C_{ox}}{q}(V_{bg} - V_T) \quad (2)$$

where V_T is the threshold voltage obtained by linear extrapolation at maximum trans-conductance for each channel (*SI Appendix*, Fig. S7b**)**. We extract $R_c \approx 6.7$ kΩ.μm at room temperature for a carrier density *n* of about 1.8×10^{12} cm^{-2}.

First-principles calculation: First-principles calculation was performed using density functional theory (DFT) within the general gradient approximation (GGA), in the form of Perdew-Burke-Ernzerhof's exchange-correlation functional. The term for van der Waals correction is included in the Kohn-Sham energy as in the form of Grimme's DFT-D2 method. The energy cutoff for the plane wave basis set was chosen to be 350 eV for all the calculations. The code is implemented by the Vienna Ab-initio Simulation Package (VASP).

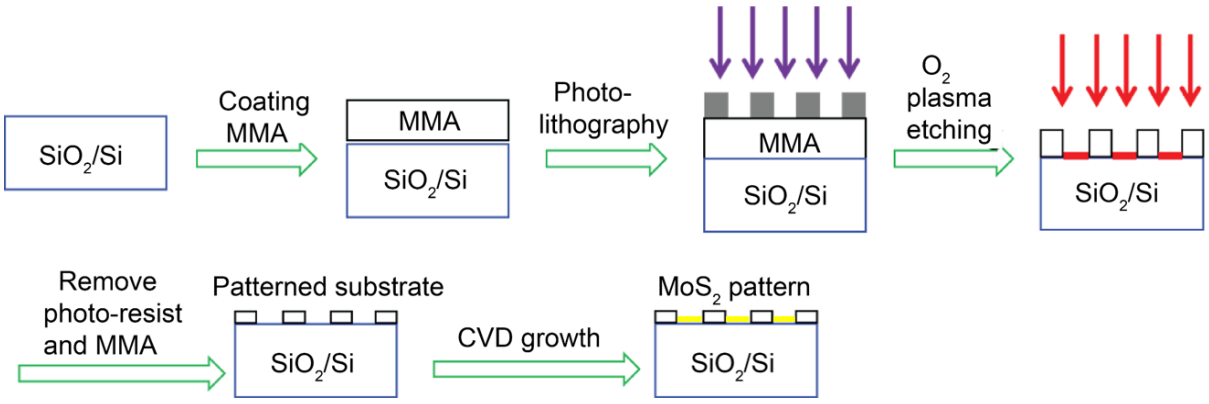

Figure S1. Schematic representation of procedure to directly grow MoS_2 patterns by modifying the growth substrate.

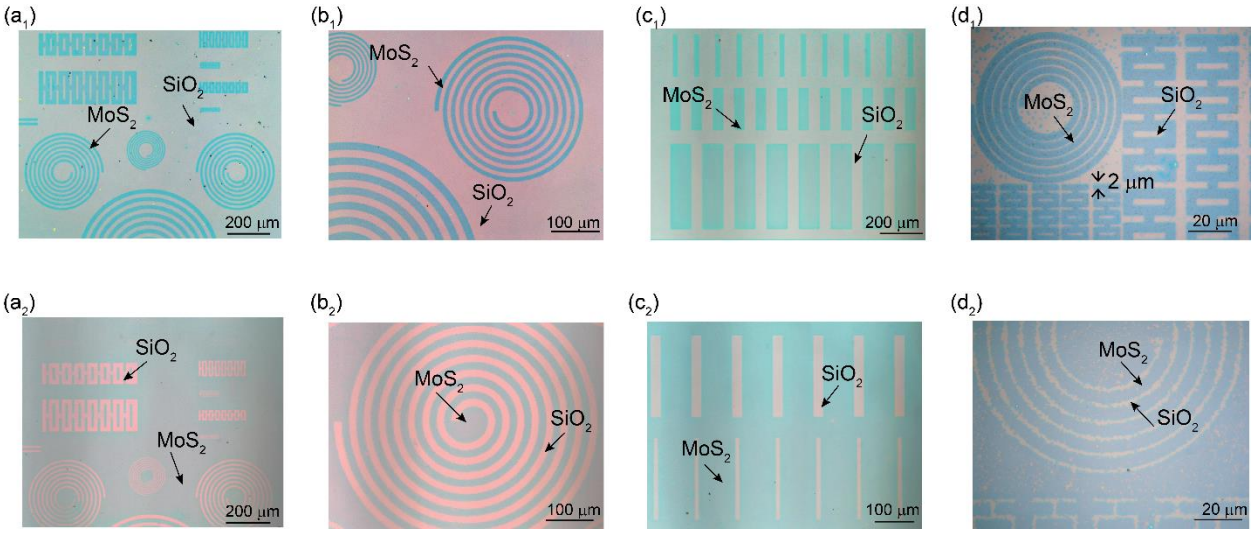

Figure S2. Optical microscope (OM) images of monolayer MoS_2 kirigami nanostructures and films. (a_1) Typical OM image of monolayer MoS_2 kirigami patterns on SiO_2/Si substrate. (a_2) Typical OM image of patterned monolayer MoS_2 film grows at the opposite locations when a negative photoresist was used for pattern in (a_1). (b_1-b_2) OM images of monolayer MoS_2 spiral patterns (b_1), and inverse MoS_2 spiral (b_2) on SiO_2/Si substrate. (c_1-c_2) OM images of monolayer

MoS_2 stripes in an 8×3 array (c_1), and inverse MoS_2 stripes (c_2) on SiO_2/Si. (d_1-d_2) OM images of monolayer MoS_2 spiral patterns (d_1), and inverse MoS_2 spiral pattern (d_2) on SiO_2/Si.

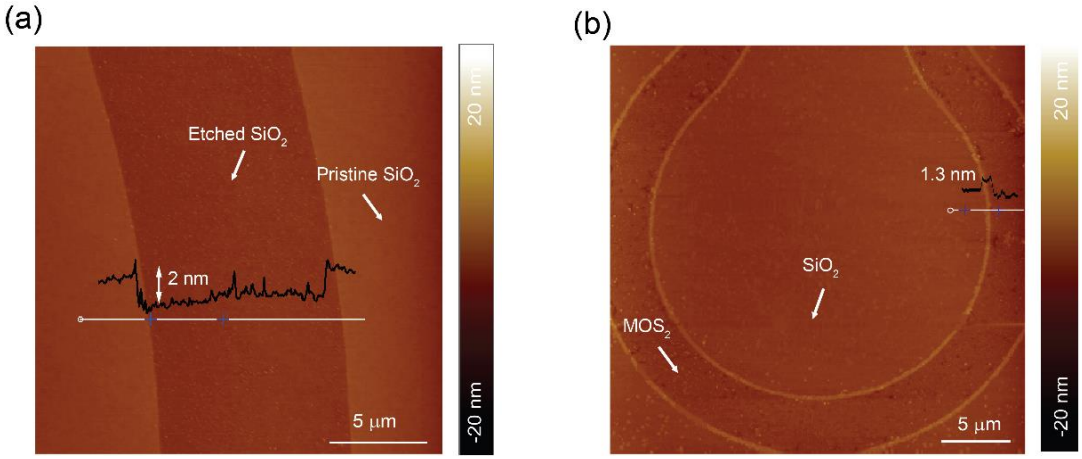

Figure S3. (a) AFM image and the corresponding height profile of the patterned SiO_2/Si substrate before MoS_2 growth. (b) AFM image and the corresponding height profile of a monolayer MoS_2 circular pattern grown on modified SiO_2/Si substrate.

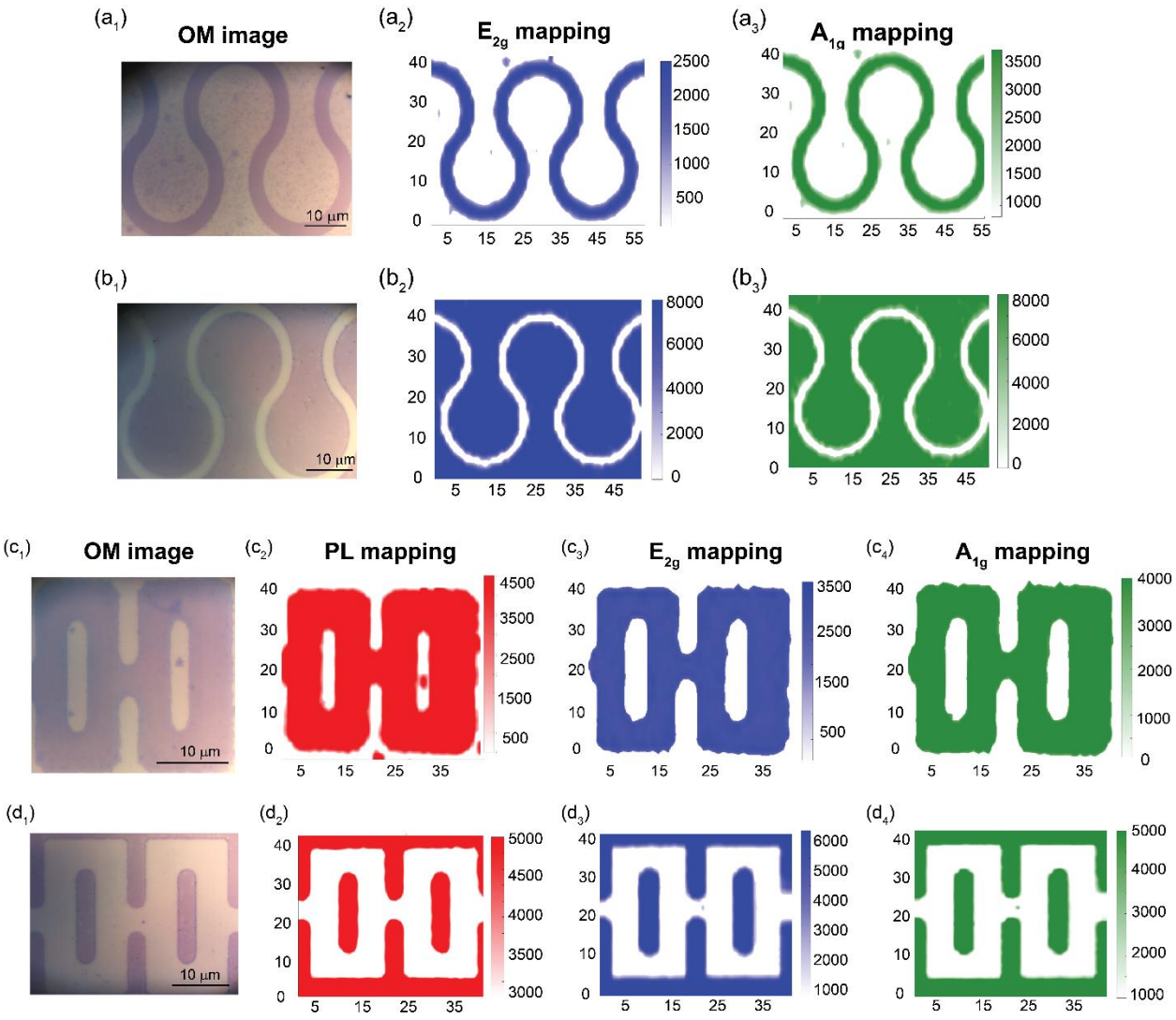

Figure S4. Optical microscope, Raman and PL spectra characterizations of the monolayer MoS_2 patterns. (a_1) OM image of a monolayer MoS_2 wave kirigami pattern. (a_2) The corresponding E_{2g} Raman mapping image of MoS_2 pattern in (a_1). (a_3) The corresponding A_{1g} Raman mapping image of MoS_2 pattern in (a_1). (b_1-b_3) OM image, E_{2g} Raman mapping and A_{1g} Raman mapping of a monolayer MoS_2 wave pattern. (c_1) OM image of a monolayer MoS_2 rectangle pattern. (c_2) The corresponding PL mapping of MoS_2 pattern in (c_1). (c_3, c_4) The corresponding Raman mappings (c_3 for E_{2g} peak and c_4 for A_{1g} peak) of MoS_2 pattern in (c_1). (d_1-d_4) OM image, PL mapping and Raman mappings of another monolayer MoS_2pattern.

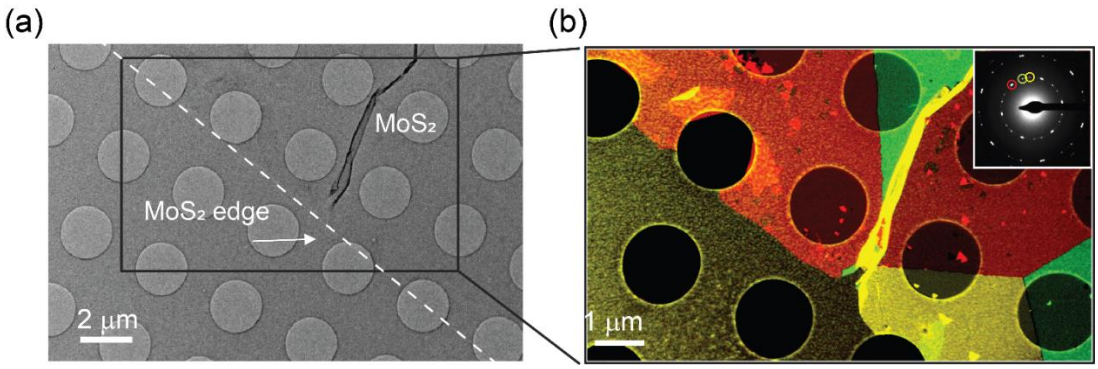

Figure S5. (a) Bright field TEM image of the edge of a monolayer MoS_2 pattern. (b) The corresponding dark field TEM image of the monolayer MoS_2 edge in (a), showing the grain size of the patterned region is greater than 5 μm. Inset: the diffraction image suggest this region is polycrystalline.

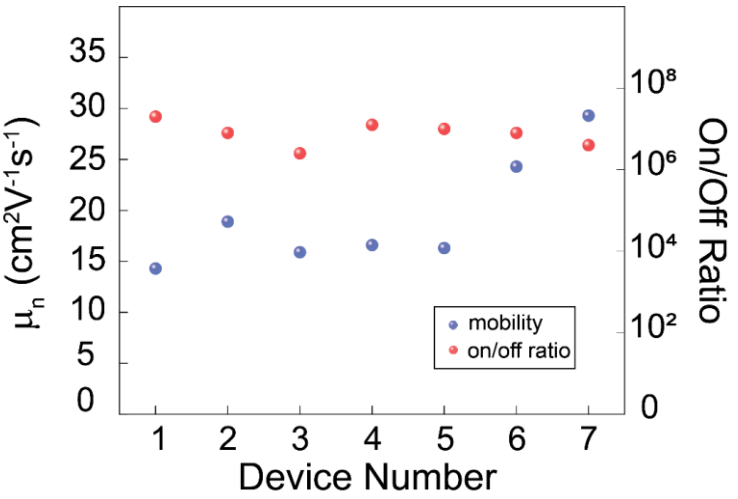

Figure S6. Electron mobility and on/off current ratio for 7 monolayer MoS_2 FETs measured in this work. All electrical measurements were carried out under ambient environment at room temperature.

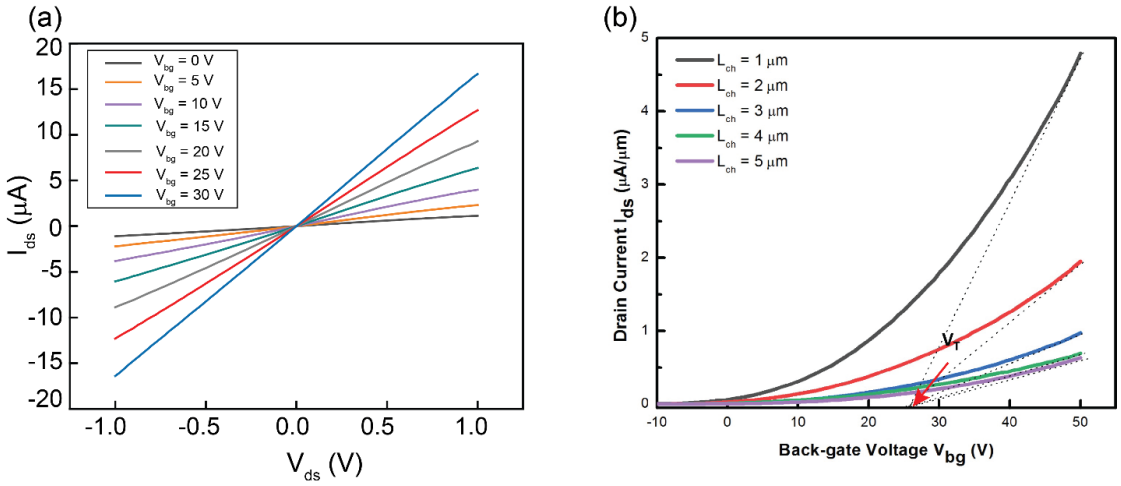

Figure S7. (a) Output (I_{ds}–V_{ds}) characteristics of the same MoS_2 transistor with gate voltages from 0 to 30 V, the linear behavior suggesting Ohmic contacts between MoS_2 and Au electrodes. (b) I_{ds}–V_{bg} characteristics of five typical transistors fabricated on the directly grown MoS_2 patterns with different channel lengths, L (1, 2, 3, 4, and 5 μm).

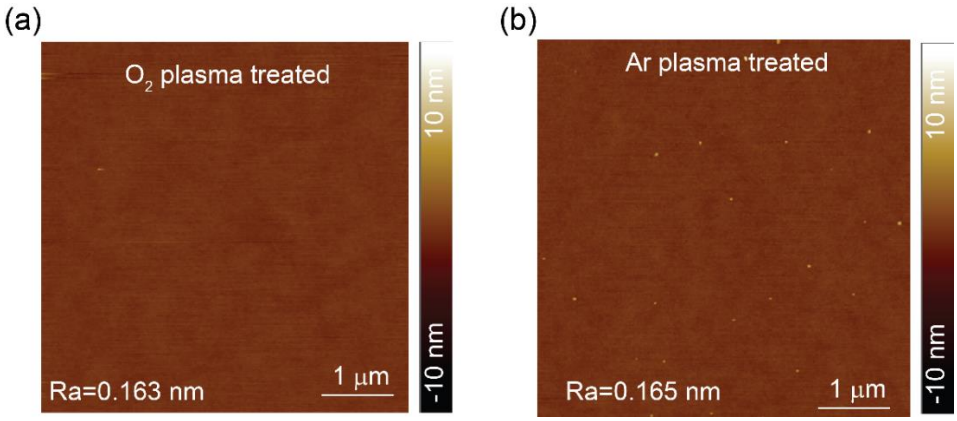

Figure S8. The comparison of surface roughness for O_2 plasma and Ar plasma treated SiO_2/Si substrates. (a) AFM height of O_2 plasma treated SiO_2/Si substrate. (b) AFM height of Ar plasma treated SiO_2/Si substrate.

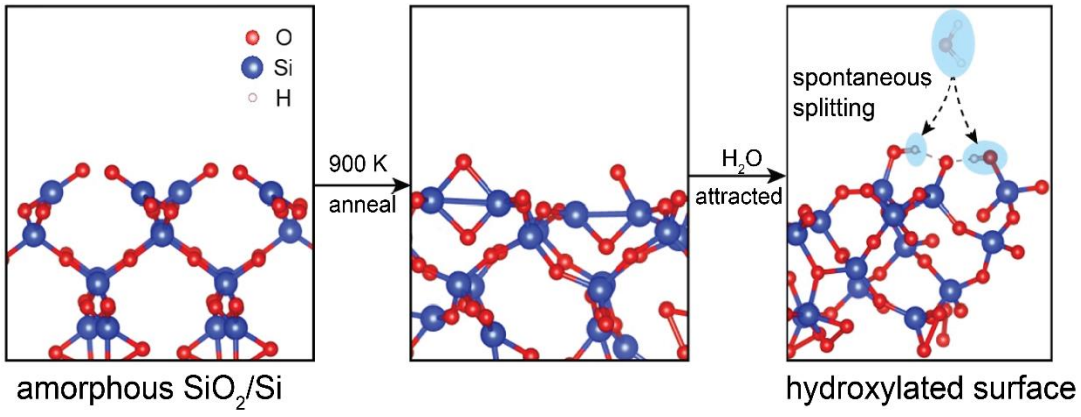

Figure S9. The hydroxylation process for amorphous SiO_2/Si substrates.

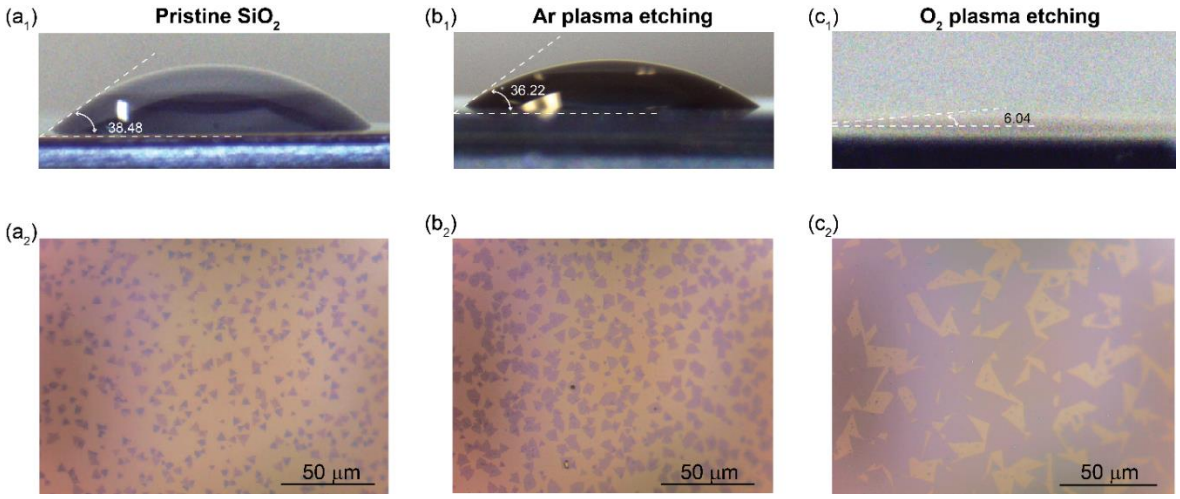

Figure S10. The contact angles of SiO_2/Si treated by different methods, and CVD growth results of MoS_2 flakes grown on corresponding treated surfaces. (a_1, a_2) contact angle for pristine SiO_2/Si substrate (a_1), and the OM image of MoS_2 grown on pristine SiO_2/Si (a_2). (b_1, b_2) contact angle for Ar plasma treated SiO_2/Si substrate (b_1), and the OM image of MoS_2 grown on Ar plasma treated SiO_2/Si (b_2). (c_1, c_2) contact angle for O_2 plasma treated SiO_2/Si substrate (c_1), and the OM image of MoS_2 grown on O_2 plasma treated SiO_2/Si (c_2). The results here indicate that

substrates with better wettability (thus higher surface energies) are more beneficial for the growth of monolayer MoS_2.

Figure S11. (a) Schematic illustration and the enlarged feature of the MoO_3 crucible covered by patterned SiO_2/Si substrate in a typical CVD growth system. (b-e) OM images of MoS_2 patterns grown on different regions (l_1-l_4) with different sulfur concentration. The sulfur concentration decreases from region l_1 in (b) to region l_4 in (e).

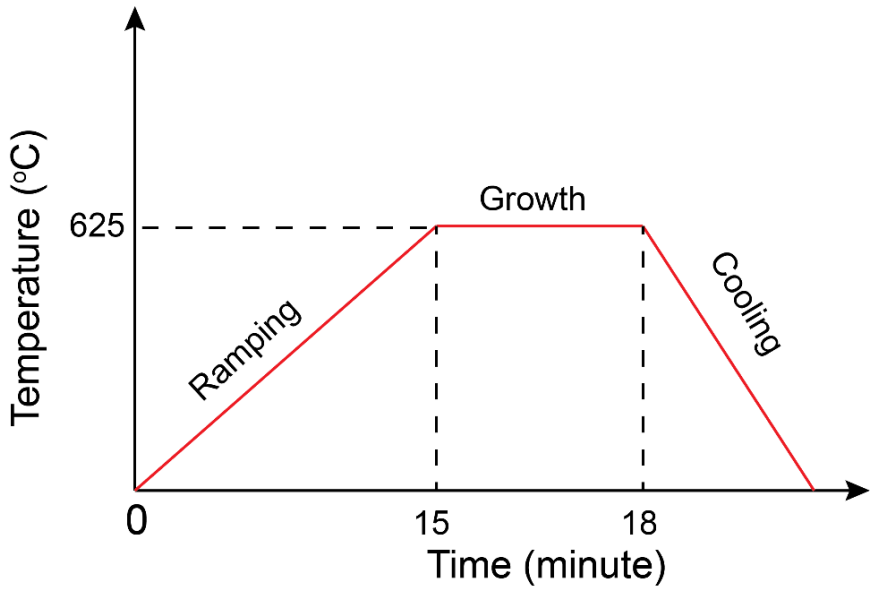

Figure S12. The temperature profile of the MoS_2 growth process used for this work.

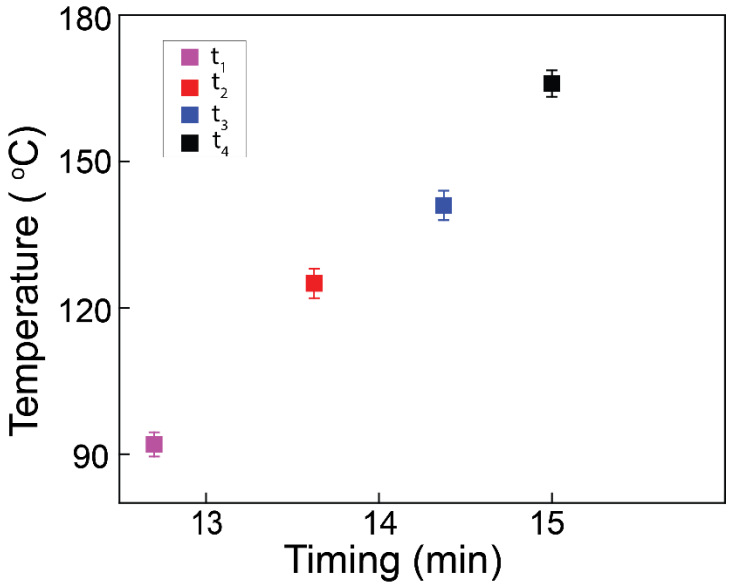

Figure S13. The relationship between the entrance timing of the sulfur precursor and the heating temperature at the corresponding location.

Table S1. Chart of the temperatures and partial pressures of sulfur and MoO_3, respectively, at different entrance timing of sulfur precursor, (formulas see in ref. 1 and 2). The distance between the left edge of furnace and the front of sulfur boat is around 1.5 cm, corresponding to "d_2" in Figure. 3*C* and Figure S14.

	t_1	t_2	t_3	t_4
T_{MoO3}	520 °C	570 °C	600 °C	625 °C
P_{MoO3}	0.135×10^{-7} atm.	4.8295×10^{-7} atm.	33.8×10^{-7} atm.	154.94×10^{-7} atm.
T_{Sulfur}	92 °C	125 °C	141 °C	166 °C
P_{Sulfur}	2.3×10^{-6} atm.	6.8×10^{-5} atm.	1.4×10^{-4} atm.	4.28×10^{-4} atm.
[S]/[MoO_3]	175.37	137.79	53	27

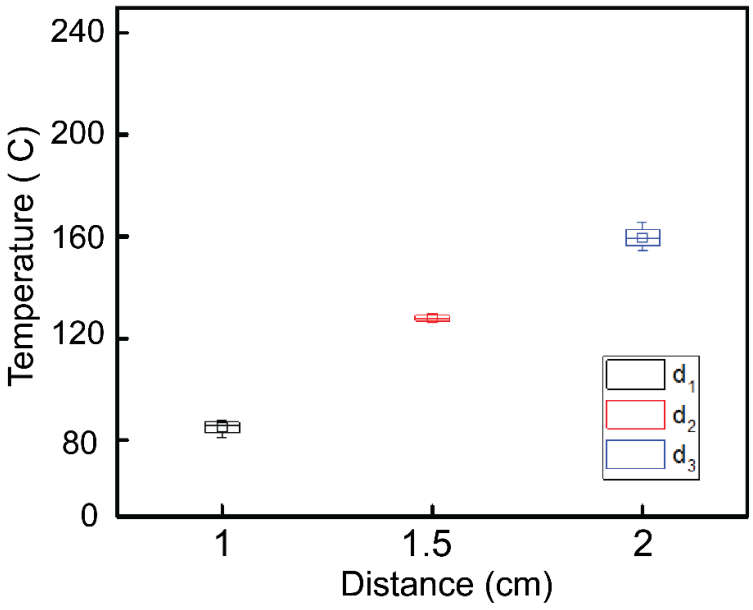

Figure S14. The relationship between the locations of the sulfur boat and the corresponding temperatures.

Table S2. The temperature, partial pressure of sulfur precursor, nucleation rate ($\dot{N}$) and growth rate ($\dot{G}$) in three dimensional (3D) and 2D of MoS_2 patterns at different offset locations of the sulfur boat. The nucleation rate and growth rate were semi-quantitatively calculated based on the following formulas[3], respectively: $\dot{N} = 2\pi r^* a_0 sin\theta \frac{PN_A}{(2\pi MRT)^{1/2}} n_s \exp\left(\frac{E_{des}-E_S-\Delta G^*}{k_B T}\right)$; $\dot{G} = \frac{MP\dot{V}}{k_B T \rho A}$ (in 3D); $\dot{G} = \frac{AMoS2/Atot}{tgrowth} \cdot h_{MoS2} \cdot A_{tot}$ (in 2D)

	d_1 (1 cm)	**d_2 (1.5 cm)**	**d_3 (2 cm)**
T_{Sulfur}	85	125	160
(P_{Sulfur})	8.968×10^{-4} tor	9.12×10^{-2} tor	0.332 tor
$\dot{N}$	0.05±0.02	0.8125±0.08	2.5±0.05
(3D) $\dot{G}$	4.75±0.9	11.4±0.8	34±0.8
(2D) $\dot{G}$	0.416±0.038	0.96±0.045	0.74±0.033

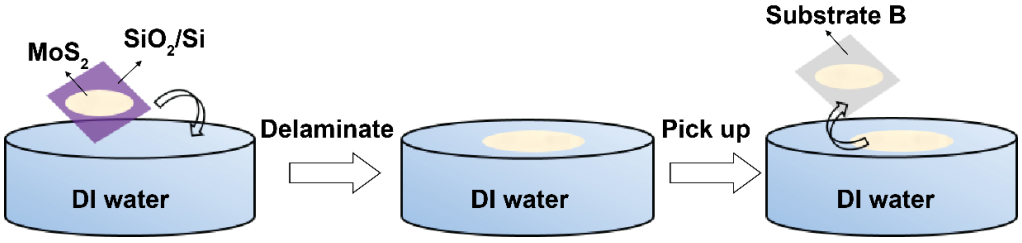

Figure S15. Schematic representation of water delamination procedures for the directly grown MoS_2 patterns.

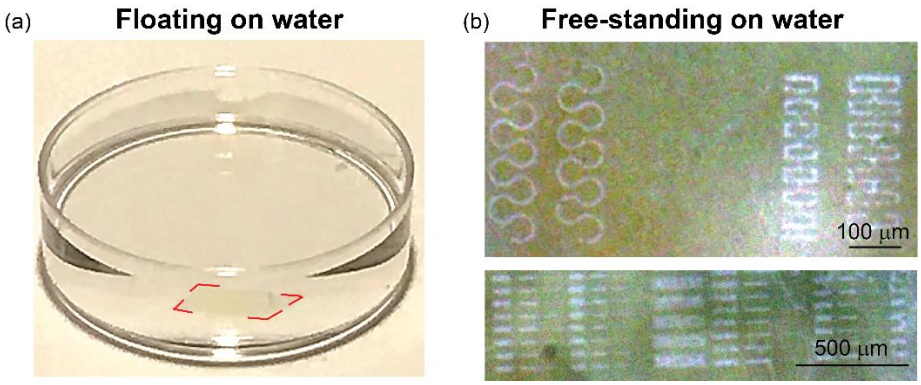

Figure S16. (a) Photograph for monolayer patterned MoS_2 film floating on the surface of water. (b) OM images of monolayer MoS_2 kirigami structures freestanding on a water surface without any additional support.

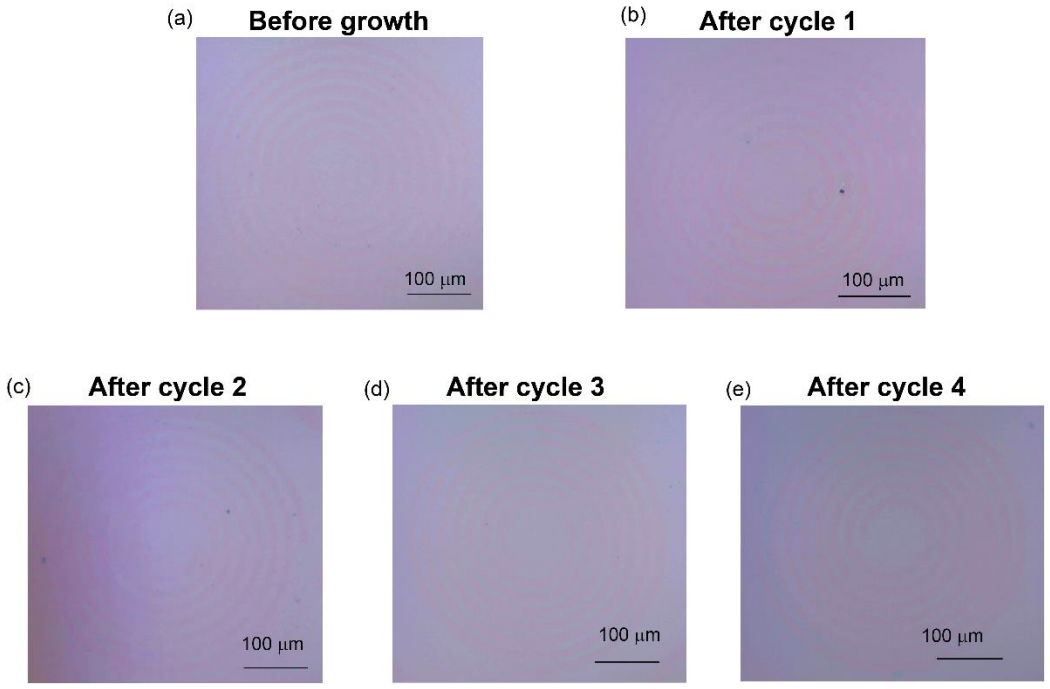

Figure S17. Water delaminating transfer and recycled growth of patterned MoS_2 nanostructures. (a) OM image of the patterned SiO_2/Si substrate before growth. (b-e) OM images

of patterned SiO_2/Si substrates after the first through fourth cycles of the water delaminating transfer.

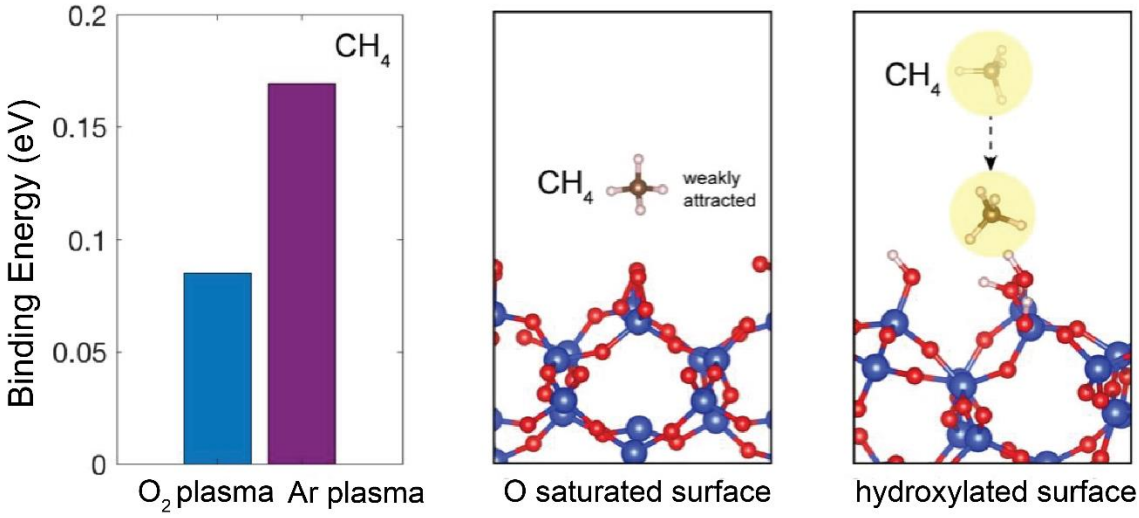

Figure S18. DFT calculation for the binding energy between amorphous carbon (to simplify the calculation, we use CH_4, which contains only one carbon atom to stand for amorphous carbon) and the growth substrates treated by O_2 plasma and Ar plasma. The O saturated surface is only weakly attractive to CH_4 molecule, while the hydroxylated surface has a higher binding energy for CH_4, indicating the O saturated surface condition is relatively more stable when compared with hydroxylated surface in air.

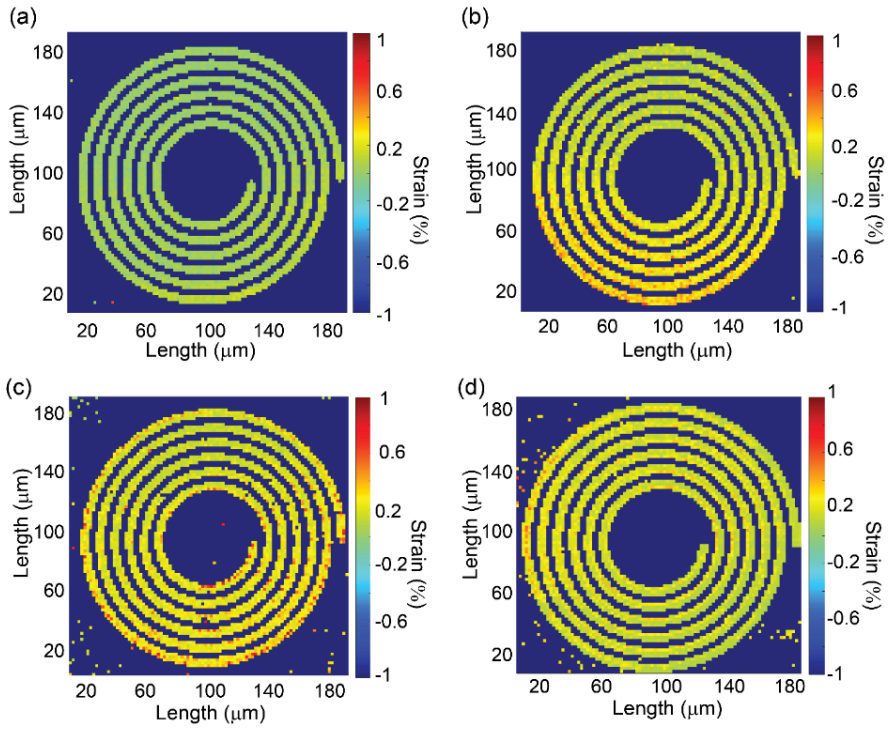

Figure S19. The strain mappings (via Raman) of monolayer MoS_2 spirals after the first through fourth growth cycles.

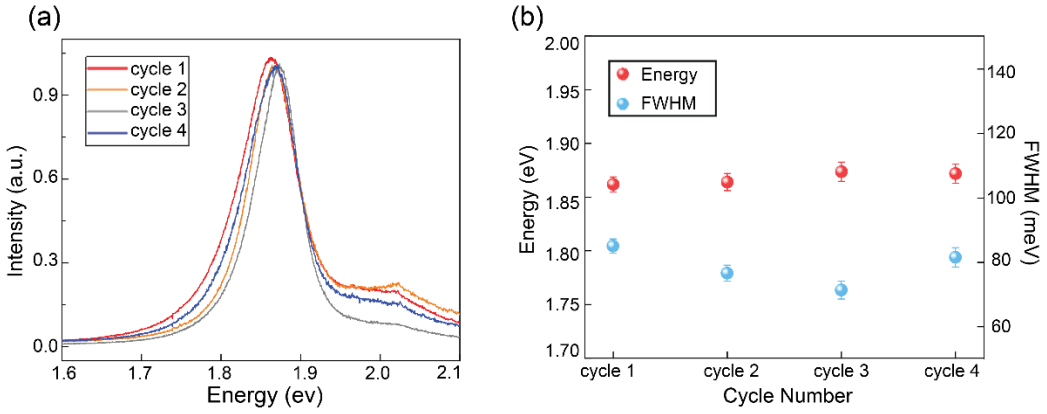

Figure S20. PL characterizations for repeated growth of monolayer MoS_2 patterns. (a) Normalized PL spectra collected on MoS_2 spiral structures in Fig. 4*F*. (b) The comparison for PL

peak energy and FWHM among samples grown in each cycle. Red dots correspond to the PL peak energy, and blue dots correspond to the FWHM of the PL.

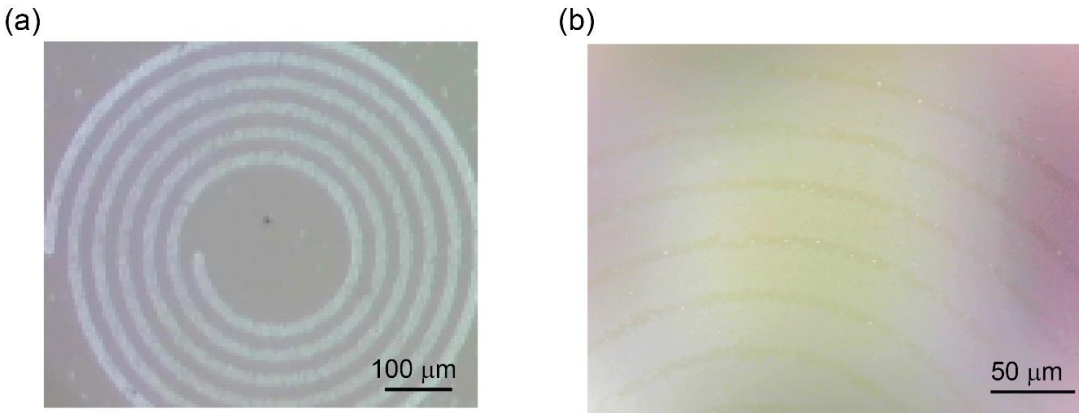

Figure S21. (a) OM image of a monolayer MoS_2 spiral spring transferred to a transparent quartz substrate. (b) OM image for monolayer MoS_2 spiral spring transferred to a transparent mica substrate.

Reference:

1. West, W. A. & Menzies, A. W. C. The Vapor Pressures of Sulphur between 100° and 550° with related Thermal Data. *J. Phys. Chem.* **33,** 1880–1892 (1928).
2. Blackburn, Paul E., Michael Hoch & Johnston Herrick L. The vaporization of molybdenum and tungsten oxides. *J. Phys. Chem.* **62**, 769–773 (1958).
3. Ohring, M. *Materials Science of Thin Films*. (Elsevier, 2001).